

MicroCT-based method for imaging microvasculature within bone tissue

Version [v1.0](#) of this manuscript was submitted to [Small Methods](#) and is available as preprint at bioRxiv with the DOI [10.1101/2023.03.08.531678](https://doi.org/10.1101/2023.03.08.531678).

The version of the manuscript you see here ([permalink](#)) was automatically generated from [microct-ana-unibe-ch/microvasculature-manuscript@a44ec66](#) on July 13, 2023. Changes to the submitted version are visualized [here on GitHub](#).

Authors

- **David Haberthür**  
[ID 0000-0003-3388-9187](#) ·  [habi](#) ·  @habi@mastodon.social
Institute of Anatomy, University of Bern, Baltzerstrasse 2, CH-3012 Bern, Switzerland
- **Oleksiy-Zakhar Khoma**  
[ID 0000-0002-1914-6873](#) ·  [ol-khoma](#)
Institute of Anatomy, University of Bern, Baltzerstrasse 2, CH-3012 Bern, Switzerland
- **Tim Hoessly**
Institute of Anatomy, University of Bern, Baltzerstrasse 2, CH-3012 Bern, Switzerland
- **Eugenio Zoni**
Department for BioMedical Research, Urology Research Laboratory, University of Bern, Bern, Switzerland; Department of Urology, Inselspital, Bern University Hospital, Bern, Switzerland
- **Marianna Kruithof-de Julio**  
[ID 0000-0002-6085-7706](#)
Department for BioMedical Research, Urology Research Laboratory, University of Bern, Bern, Switzerland; Department of Urology, Inselspital, Bern University Hospital, Bern, Switzerland; Department for BioMedical Research, Translation Organoid Research, University of Bern, Bern, Switzerland
- **Stewart D. Ryan**  
[ID 0000-0001-7016-771X](#)
U-Vet Hospital, University of Melbourne Veterinary School, Werribee, Australia
- **Myriam Grunewald**  
[ID 0000-0001-5394-9218](#)
Department of Developmental Biology and Cancer Research, Faculty of Medicine, The Hebrew University, Organoid Research Center, Hadassah University Hospital, Jerusalem, Israel
- **Benjamin Bellón**  
[ID 0000-0003-2297-9160](#)
Preclinical and Translational Research, Institut Straumann AG, Basel, Switzerland
- **Rebecca Sandgren**  
[ID 0000-0003-4473-4666](#)
Centre for Comparative Medicine, Medical Faculty, Lund University, Lund, Sweden

- **Benjamin E. Pippenger**

 [0000-0001-7990-5555](#)

Preclinical and Translational Research, Institut Straumann AG, Basel, Switzerland; Department of Periodontology, University of Bern, Bern, Switzerland

- **Dieter Bosshardt**

 [0000-0002-2132-6363](#)

Department of Periodontology, University of Bern, Bern, Switzerland

- **Valentin Djonov**

 [0000-0002-5062-1169](#)

Institute of Anatomy, University of Bern, Baltzerstrasse 2, CH-3012 Bern, Switzerland

- **Ruslan Hlushchuk** 

 [0000-0002-6722-8996](#)

Institute of Anatomy, University of Bern, Baltzerstrasse 2, CH-3012 Bern, Switzerland

⌚ — David Haberthür and Oleksiy-Zakhar Khoma contributed equally to this work.

✉ — Corresponding author: Ruslan Hlushchuk (ruslan.hlushchuk@unibe.ch, [+41 31 684 46 80](tel:+41316844680)).

Abstract

Angiogenesis is essential for skeletal development, bone healing and regeneration. Improved non-destructive, three-dimensional (3D) imaging of the vasculature within bone tissue would benefit a multitude of research areas, especially implantology and tissue engineering.

X-ray microtomography (microCT) is a well-suited non-destructive 3D imaging technique for bone morphology. For microCT-based detection of vessels, it is paramount to use contrast-enhancement. Limited differences in radiopacity between perfusion agents and mineralized bone make their distinct segmentation problematic and has been the major drawback of contrast-enhanced microCT imaging. A decalcification step resolves this issue but inhibits simultaneous assessment of bone microstructure and vascular morphology. Moreover, the problem of contrasting becomes further compounded in samples with metal implants.

This study describes μ Angiofil-enhanced microCT-based visualization of vasculature within bone tissue in small and large animal models, with and without decalcification. We present simultaneous microvascular and bone imaging in murine tibia, murine bone metastatic model, pulp chamber, gingiva and periodontal ligaments. In a large animal model (minipig) we perform visualization and segmentation of different tissue types and vessels in the hemimandible containing metal implants.

Our manuscript introduces the first non-destructive approach for 3D imaging of the vasculature within soft and hard tissues in the vicinity of metal implants in a large animal model.

Introduction

Angiogenesis, the formation of new blood vessels from preexisting vessels, is crucial for skeletal development as well as for bone healing and regeneration^[5]. In addition to carrying nutrients and growth factors, those newly formed blood vessels are a delivery route of stem cells and progenitor cells to the bone-defect site^[6-8]. In the case of bone grafts, many of the synthetic ones fail to bridge critically sized defects due to their inability to promote vascularization^[4,9]. The structural nature of skeletal tissue makes three-dimensional (3D) imaging of its vasculature extremely difficult. Histology, a destructive and two-dimensional approach, still remains a gold standard for assessing vasculature in bones^[10].

Classic soft tissue imaging techniques such as light sheet microscopy or confocal laser scanning microscopy face challenges in their application due to the encasement of blood vessels in calcified tissue^[10]. Despite recent advances in tissue clearing-based imaging methods for craniofacial bones^[11,12], the application of such methods remains challenging and is limited to small animal models. Simultaneous non-destructive 3D imaging of the vasculature within bone tissue and of the bone tissue itself, especially in the case of larger bone grafts, has been a challenge for decades^[4,13]. Thus, many research areas benefit from an improved three-dimensional (3D) imaging of the vasculature within bone tissue, for example: bone biology, bone metastatic disease, tissue engineering, implantology, and reconstructive surgery.

In the last decades, X-ray micro-computed tomography (microCT) gained recognition as a non-destructive 3D imaging technique for bone morphology^[14]. Due to the inherently low difference in X-ray absorption levels between vessels and different soft tissues it is not easily feasible to distinguish such structures within the bone. To unambiguously detect vasculature within bone it is thus necessary to instill the vessels with either a contrast agent or use a casting method to otherwise fill the blood vessels. Currently existing protocols for imaging the vasculature within the bone via vascular replica have drawbacks, like showing disjoint vascular components or completely missing vascular segments^[10,15]. The minor contrast difference between the perfusion agent to generate the replica of the vascular network and the mineralized bone makes it problematic to distinguish bone tissue and vasculature. To enable proper visualization and segmentation of vasculature within bone tissue, decalcifying the bone samples has become practically a standard method^[2,10]. Such a decalcification procedure makes simultaneous assessment of bone microstructure and vascular morphology impossible^[10].

Intravascular contrast-agent-enhanced microCT has the potential to overcome these issues. It has become a method of choice for the evaluation of angiogenesis in bone tissue engineering and remodeling applications^[2,4,16]. Barium sulfate and Microfil have been applied as the two most common contrast agents in studies on the vascularization of bone tissue. Only some selected studies^[2] managed to show better perfusion and thus visualization when perfusing the vasculature with barium sulfate. Previous studies have reported disadvantages associated with barium sulfate suspensions, including higher viscosity, which can sometimes result in incomplete vascular filling and weak or inhomogeneous signal, particularly in higher resolution scans^[2]. These issues may be attributed to particle aggregation, as indicated by various studies^[17-19]. Although Microfil has probably been applied in a larger number of vasculature imaging studies than barium sulfate, Microfil was reported to have disadvantages like vascular damage^[20] as well as poor or incomplete filling of the vasculature^[2,18,19].

In the study of tumor models^[21], assessing and non-destructively imaging tumor vasculature in 3D is a demanding task. Due to the intraosseous location, imaging is even more challenging in a bone metastatic disease model. Changes in bone and vasculature are of crucial importance for the progression of bone metastatic disease. Therefore, simultaneous imaging of bone and vasculature is

highly desired, making a decalcification step unfavorable. It is thus of a paramount importance to develop an imaging method for the assessment of tumor vasculature in the bone without decalcification, which renders bone microstructure X-ray transparent. In this manuscript, we present such a method for visualizing intratumoral vasculature and defects in mineralized bone tissue.

The craniofacial skeleton, including the mandible, is a frequent location for distraction osteogenesis as well as other forms of bone regeneration and repair, for which vascularization is important^[5,22]. Even though metal implants have revolutionized the treatment of patients with missing teeth or injured joints and bones^[23,24], they are problematic for tomographic image acquisition. The problem of imaging the vasculature becomes even further compounded in their presence, for example when studying vascularization in a jaw with metal implants. Due to their high X-ray absorption, metal implants produce beam hardening, partial volume and low signal artifacts in the resulting tomographic datasets^[25]. Interactions occurring at the tissue-implant interface are widely believed to play a crucial role in the success of implant placement and healing^[23,26]. High resolution tomographic imaging of the tissue-implant interface is complicated due to the aforementioned artifacts from the metal implants. Imaging with increased acceleration voltage and at small resolutions alleviates these imaging artifacts. MicroCT imaging is the only available approach to non-destructively investigate the intact bone-implant interface in both 3D^[23] and in proximity to the implant surface (i.e. closer than 100 µm). The Göttingen Minipig is widely recognized as a valuable large animal model in preclinical dental and orofacial research, mainly because of its anatomical similarities to humans^[27-29]. Its bone structure and bone remodeling processes closely resemble those of humans, further enhancing its suitability for such studies, including ours.

The present study introduces a technique for high-resolution microCT-based visualization of microvasculature within bone tissue in small and large animal models, both with and without decalcification of the bone. Moreover, we show that the polymer-based contrast agent µAngiofil is suitable for simultaneous imaging and subsequent analysis of peri-implant hard and soft tissues as well as their vascularization in the vicinity of metal implants in a large animal model.

Materials, Methods and Results

Animals

In this study we used one transgenic VEGF male 21 months old mouse (see^[30] for more details), 6 weeks old CB17SCID male mice, 12 weeks old C57BL/6 mice and two Göttingen minipigs. Animal procedures were performed in accordance with the applicable Swedish, Israeli or Swiss legislation on the protection of animals and were approved by the corresponding committees.

The murine experiment were approved by the local ethical committee of the Canton of Bern, Switzerland under the permit number BE 55/16. Minipig experiments were approved by the Malmö/Lund regional ethical committee, Sweden under license 5.8.18-15672/2019.

Contrast-enhanced microangioCT of mice using μAngiofil

The contrast agent μAngiofil (Fumedica AG, Switzerland) was prepared according to the manufacturer's recommendations. The perfusion of the mice was performed as previously described^[31,32]. Briefly, heparinized animals were deeply anesthetized, the thorax and the peritoneal cavity were opened with scissors to expose the descending aorta. The exposed aorta was then cannulated in either antegrade (for the perfusion of the hind limbs) or retrograde direction (for the perfusion of the head and teeth) with a Venflon cannula (26 GA). Afterwards, the blood was flushed out with warm PBS solution. Several cuts of the liver edge allowed for effusion of the blood and buffer solution. Thereafter, the selected part of the body (hind limbs or head and teeth) was perfused with μAngiofil at 1–1.5 ml/min using a syringe pump. The perfusion lasted until the organ of interest appeared completely blue^[32,33]. In bones, it is not possible to visually monitor this color change, thus perfusion of the neighboring soft tissues serves as an indirect marker of sufficient perfusion within the bone. To achieve correct perfusion of the vessels within the bone, we prolonged the perfusion time by instilling at least 2 ml of extra volume of contrast agent after all the superficial tissues of the extremity or head turned blue. After μAngiofil polymerization we fixed the samples by immersion in 4% paraformaldehyde (PFA) solution at 4° C and stored in PFA until tomographic imaging. Samples were then imaged using a SKYSCAN 1172 (Bruker microCT, Kontich, Belgium). For imaging, the samples were removed from the PFA solution, wrapped in closed-pore foam and scanned in a custom-made sealed plastic sample holder in wet atmosphere. This scan was performed on a SKYSCAN 1172 with an X-ray source acceleration voltage of 49 kV and an X-ray source current of 200 μA. Projection images were recorded over a sample rotation of 360°, with one projection acquired at each 0.05° and 3 projections being averaged for noise reduction. Each projection image with a size of 4000 x 2672 pixels was exposed for 985 ms. This resulted in an isometric voxel size of 2.99 μm. All relevant scanning and reconstruction parameters for each dataset shown in each figure are given in the [Supplementary Materials](#).

Figure 1 shows the bone microstructure and vascularization of a tibia of a 21-month-old VEGF transgenic male mouse. This visualization approach enables a simultaneous display of bone and its vascularization. These tomographic datasets were also used in another study^[30], where we performed simultaneous quantification of vasculature and bone volume.



Figure 1: microangiCT of proximal murine tibia of a 21-month-old VEGF transgenic male mouse. After perfusion with μ Angiofil the murine tibia was harvested, fixated in 4% PFA and imaged by microCT. Arrowheads mark microvessels within the tibia. The diameter of the tibia shaft is around 1 mm. On the right side of the image one can distinguish the bigger epiphyseal vessels. The bone tissue appears white at the plane of the virtual section through the microCT-dataset.

Decalcification of the μ Angiofil-perfused murine tibia

We successfully established a bone-decalcifying protocol (for murine hind limb) with 10% ethylenediamine tetra-acetic acid (EDTA) solution^[34] by adapting previous work^[15].

Decalcification of bone tissue does not negatively influence the bone structure itself, but reduces the X-ray absorption of bone tissue and thus makes it impossible to visualize it simultaneously with the vasculature (Fig. 2 B).

As described above, we instilled the lower body of 6 weeks old CB17SCID male mice with μ Angiofil. After polymerization of the contrast agent, hind limbs were collected, fixed in 4% PFA and stored in PFA until scanning. After a first scan the hind limbs were decalcified over 7 days in 10% EDTA (pH 7.5) at room temperature and then a second scan was performed.

These samples were imaged with a SKYSCAN 1172, with an X-ray source acceleration voltage of 59 kV and an X-ray source current of 167 μ A. The X-rays were filtered by 0.25 mm of aluminum prior to incidence onto the sample. Projection images were recorded over a sample rotation of 180°, with one projection acquired at each 0.1° and 2 projections being averaged for noise reduction. Each projection image with a size of 4000 x 2672 pixels was exposed for 1740 ms. This resulted in an isometric voxel size of 3.19 μ m.



Figure 2: microangioCT-based visualization of the diaphysis of CB17SCID mice tibia before (A & A') and after decalcification with 10% EDTA (B & B'). In A and A' the tibia bone appears brighter and opaque due to higher X-ray absorption. In B and B' the tibia bone appears transparent due to its lowered X-ray absorption after decalcification. Due to the decalcification, connecting vessels between the periosteal vessels and the vessels of the bone marrow cavity (bmc) are more easily detectable (blue arrows in A vs. B). The visualization of the vessels within the medullar cavity (*central sinus* (CS)) is also improved. At the external surface of the tibia, supplying arteries are visible (*arteria et vena nutricia* (avn)).

Bone metastatic disease model, microangioCT

As mentioned in the introduction, simultaneous imaging of bone and vasculature is crucial in a bone metastatic disease model. Since changes in bone and vasculature are believed to be of crucial importance for the progression of bone metastatic disease, decalcifying the bone tissue is highly unfavorable.

To verify the suitability of our microangioCT approach for imaging intratumoral vasculature in native, non-decalcified bone tissue we used the following murine bone metastatic disease model. 50000 PC3-M-Pro4Luc2 dTomato cells were injected into the tibia of 6 weeks old CB17SCID male mice as previously described^[35,36]. The X-ray assessment (25 kV, 6 sec, Faxitron Bi optics, Tucson, Arizona, US) was conducted at days 7, 14, 21 and 28 after implantation to monitor the progression of the lesions. Prior to terminal anesthesia and perfusion with μAngiofil as described above, the hind limb of interest was X-rayed using Faxitron Bi optics as a standard follow-up in this model (see insert in Fig. 3, Panel A). The harvested and fixated murine hind limb (4% PFA at 4° C) was then imaged using a desktop microCT scanner SKYSCAN 1272 (Fig. 3), with an X-ray source acceleration voltage of 60 kV and an X-ray source current of 166 μA. The X-rays were filtered by 0.25 mm of aluminum prior to incidence onto the sample. Projection images were recorded over a sample rotation of 180°, with one projection acquired at each 0.1° and 3 projections being averaged for noise reduction. Each projection image with a size of 4904 x 3280 pixels was exposed for 2800 ms. This resulted in an isometric voxel size of 1.65 μm.

The visualization (CTvox (v.3.3.1, microCT Bruker, Kontich, Belgium)) unambiguously displays intratumoral vasculature and extensive defects in mineralized bone tissue. Neighboring structures, such as the growth plate and the epiphysis or the menisci are also easily assessed (Fig. 3).

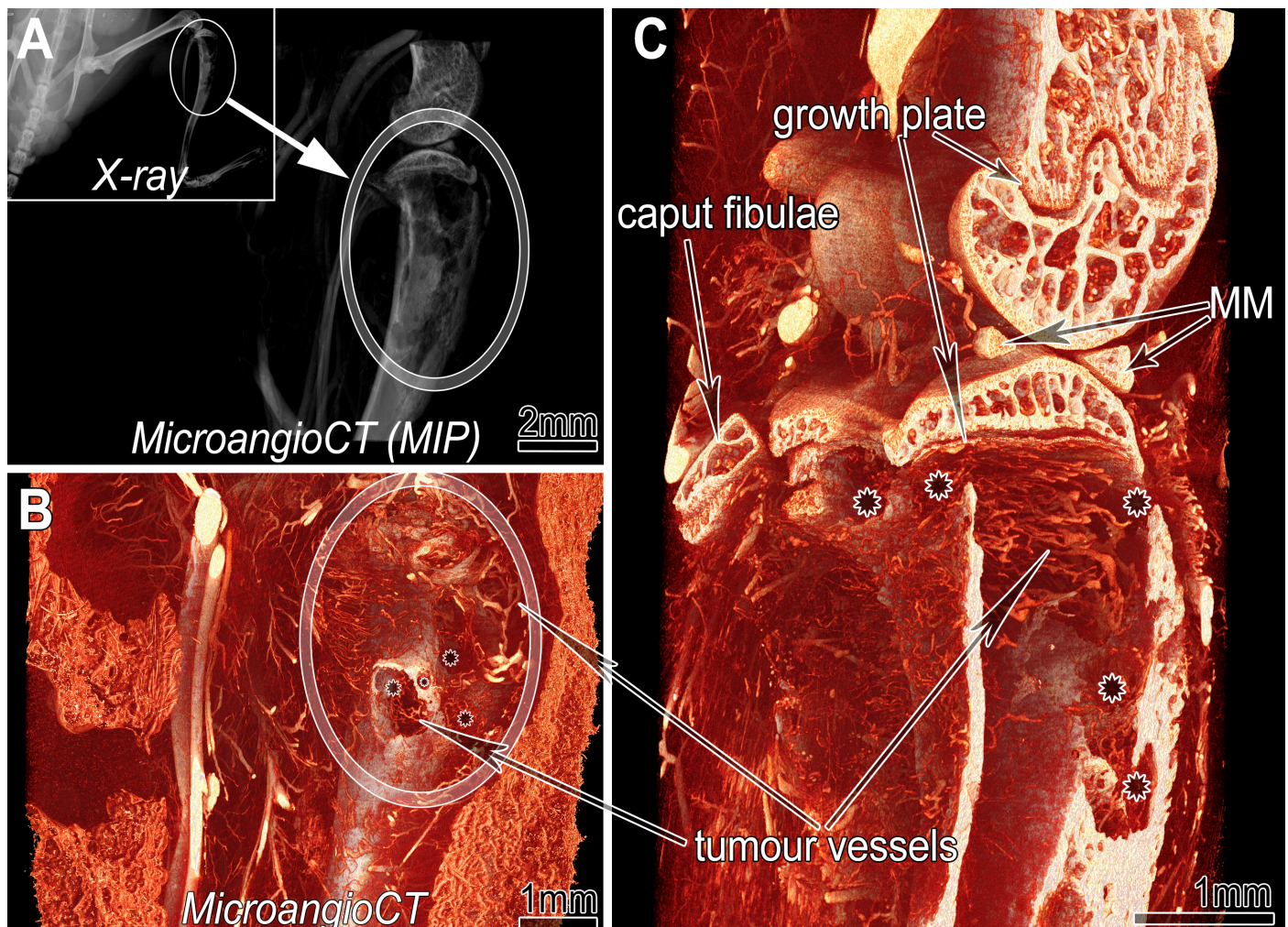


Figure 3: microangioCT of a xenograft tumor implanted into tibia of 6 weeks old CB17SCID male mice. A: Maximum intensity projection (MIP) of the three-dimensional dataset of the investigated hind limb segment indicated in the inserted X-ray image of the mouse prior harvesting. Inset: X-ray image prior to terminal anesthesia. B: Virtual section through the microangioCT dataset visualizing remarkable defects represented as holes (asterisks in B and C) in the tibial bone at the tumor site (encircled). C: A more deeply positioned virtual section displaying the inner surface of the diseased tibia. Besides irregularly patterned tumor vessels (in B & C) further bony structures like growth plate or calcified parts of the medial meniscus (MM) are clearly distinguishable.

microangioCT of murine mandible and teeth

C57BL/6 mice were terminally anesthetized and their head was perfused with μ Angiofil as described above. The perfused head was harvested and fixed (4% PFA at 4° C). Prior to tomographic imaging the mandible was excised, wrapped in a paper towel and scanned in a sealed pipette tip. The mouse teeth were imaged using a desktop microCT scanner SKYSCAN 1172 (Fig. 4), with an X-ray source acceleration voltage of 80 kV and an X-ray source current of 124 μ A. The X-rays were filtered by 0.5 mm of aluminum prior to incidence onto the sample. Projection images were recorded over a sample rotation of 360°, with one projection acquired at each 0.1° and 4 projections being averaged for noise reduction. Each projection image with a size of 4000 x 2672 pixels was exposed for 6260 ms. This resulted in an isometric voxel size of 1 μ m.

The microvasculature of murine mandible, periodontal ligament, and the teeth (even within their pulp chamber) can be clearly visualized without undergoing a decalcification procedure (Fig. 4).





Figure 4: microangioCT of the vasculature of C57BL/6 mice teeth. A: View onto a virtual section parallel to the crowns of the murine teeth: pulp chambers are visible, and the pulpal vessels are presented. The inset shows an full view of the tomographic dataset. B: Sagittal section through the mandible. The microvessels within the pulp cavities and root canals are distinguishable. C: Detailed view of the dentogingival plexus and periodontal ligament vessels (PLV).

microangioCT of mandible in a large animal model (Göttingen Minipig)

Göttingen minipigs (Ellegaard Göttingen Minipig, Dalmose, Denmark) were anesthetized intramuscularly (25–35 mg/kg, Dexdomitor; Orion Pharma Animal Health and 50–70 mg/kg, Zoletil 100 Vet, Virbac) and intravenously heparinized with 300 IE/kg (Heparin LEO, LEO Pharma). After heparin infusion, the pigs were euthanized with an intravenous dose (100 mg/kg) of pentobarbital (Euthanimal vet, VM Pharma). The external carotid artery was accessed by blunt dissection through tissue of the ventral neck and cannulated (BD Venflon, 17G). After washing out the blood with PBS, the corresponding head side was selectively perfused with μ Angiofil through the arterial tree. The perfusion was visually monitored equivalent to the previously described perfusion in mice. After polymerization of μ Angiofil we excised the mandible and fixated and stored it in 4% PFA solution at 4° C.

Mandibles were then scanned with a SKYSCAN 1273 (Fig. 5). The scans were performed with an X-ray source acceleration voltage of 100 kV and an X-ray source current of 80 μ A. The X-rays were filtered by 1 mm of aluminum and 0.2 mm of copper prior to incidence onto the sample. For the visualization shown in panel A, we recorded projection images with a size of 3072 x 1944 pixels over a sample rotation of 360°, with one projection acquired at each 0.1° and 5 projections being averaged for noise reduction. Each projection image was exposed for 225 ms. This resulted in an isometric voxel size of 21 μ m. For the visualizations shown in panels B and C, the sample was rotated over totally 360° with one projection acquired at each 0.15° and 5 projections were averaged. In addition, two horizontally overlapping projections were stitched to one projection with a size of 4832 x 1944 px to increase the imaged sample volume. Each projection image was exposed for 225 ms. This resulted in an isometric voxel size of 9 μ m.



Figure 5: microangioCT of the minipig mandibula. Panel A displays the visualization of a right minipig hemimandible. The vasculature at the bone surface is clearly visible. The framed area in A marks the subvolume represented in panel B at higher magnification. Panel C displays the transverse section marked in panel B: the pulp chamber and root canal with the corresponding vessels are unambiguously visualized. Due to the voxel size of 8–9 μm , microvessels with diameter of 40 μm or less cannot be visualized in such large samples.

Osseointegration of implants is influenced by angiogenesis. As such, studying angiogenesis and, correspondingly the vascular supply of the peri-implant tissue in detail is important for dental research and many implantology studies. So far, the only reliable approach to assess the vascular supply remains histology, limited to single two-dimensional sections.

While microCT imaging allows for non-destructive, fully 3D imaging of dental research samples with implants, such imaging is a challenging task due to the presence of these metal parts with high density and X-ray absorption within the samples. A decalcification step reduces the density of the sample but inevitably leads to the loss of information on the bone microstructure making the simultaneous assessment of the bone and vessels impossible^[10]. For distinguishing the vasculature

from both the metal implants and the mineralized bone tissue, the vasculature has to be instilled with a suitable contrast agent. The X-ray absorption characteristics of μ Angiofil make it possible to visualize and distinguish between soft tissue, bone tissue, contrast agent-filled vessels as well as metal implants according. We imaged an μ Angiofil-instilled minipig hemimandibula with a SKYSCAN 2214 (Fig. 6), with an X-ray source acceleration voltage of 100 kV and an X-ray source current of 100 μ A. The X-rays were filtered by 1 mm of copper prior to incidence onto the sample. Projection images were recorded over a sample rotation of 360°, with one projection acquired at each 0.18° and 4 projections being averaged for noise reduction. Each projection image with a size of 2929 x 1944 pixels was exposed for 1080 ms. This resulted in an isometric voxel size of 8 μ m.

In the resulting tomographic datasets these regions of interest can easily be distinguished based on their gray values ranges, as shown in Fig. 6, Panel C. Tomographic imaging of such samples and straightforward segmentation of features of interest without cumbersome post-processing (Fig. 6, Panel D) is enabled without requiring a decalcification step.

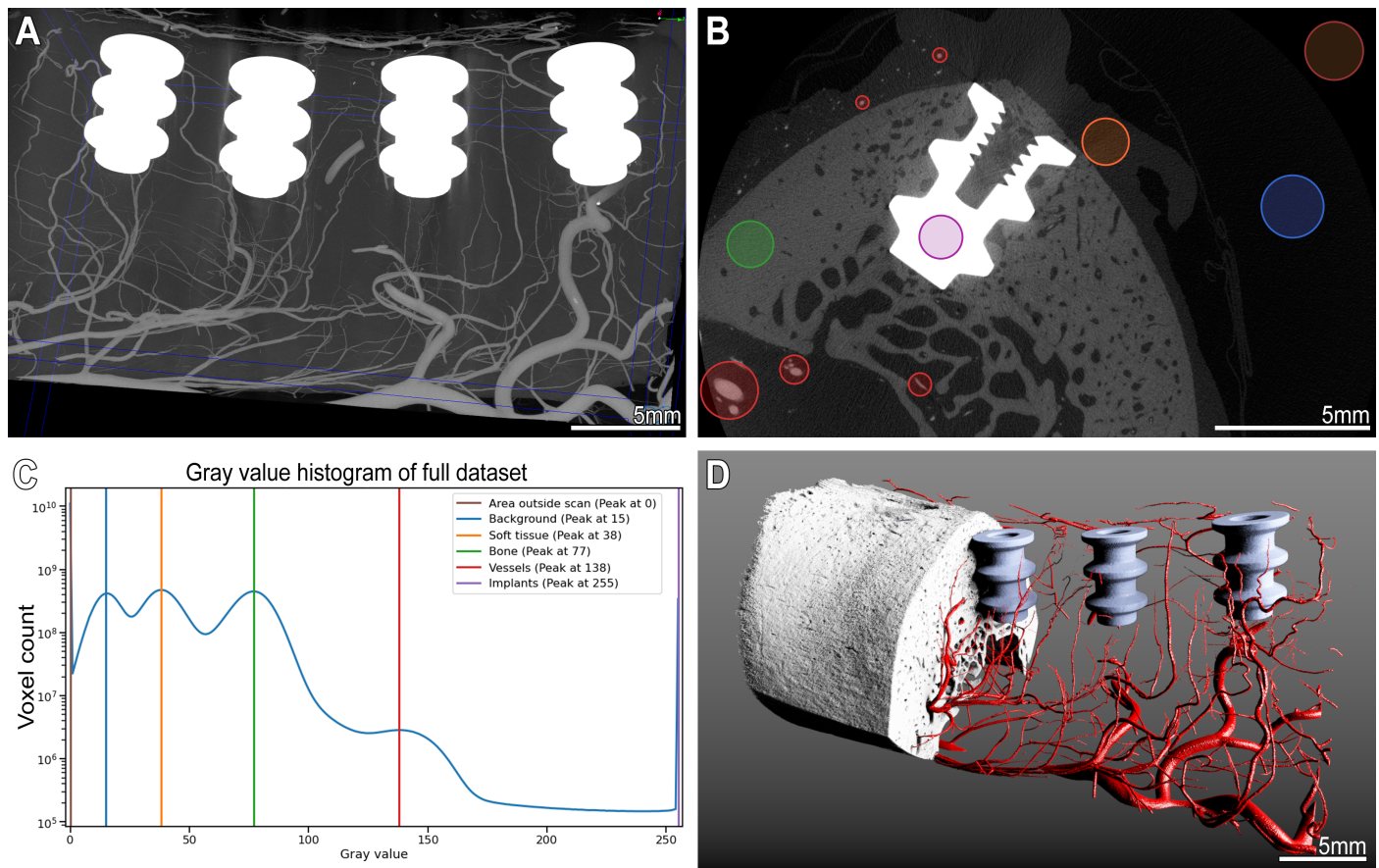


Figure 6: microangioCT of the peri-implant vasculature of a minipig mandibula. Panel A: Maximum intensity projection image of the minipig mandible dataset with 4 metal implants and μ Angiofil-perfused vessels. Panel B: virtual transversal section through the dataset showing an implant within the mandible. The colored circles mark structures with different gray values ranges. Corresponding peaks with color legend are marked on the histogram in panel C. Such differences in gray levels allow a straightforward segmentation of the structures of interest as displayed in the 3D visualization in panel D.

Discussion

Adequate vascularization is a prerequisite for successful bone formation and regeneration as well as osseointegration of biomaterials^[1,37–40]. Without high-resolution imaging, the interplay between vasculature and bone tissue cannot be adequately studied, making it impossible to control these processes.

Non-destructive microCT imaging is considered the only viable approach for 3D imaging of an intact bone-implant interface^[23]. To properly distinguish the vasculature from other soft tissue structures, instillation of a contrast agent or producing an intravascular casting is necessary.

Our hereby presented method of imaging the microvasculature within bones based on instillation with μ Angiofil overcomes several drawbacks of previously described methods (see [Introduction](#) for a thorough explanation) and is suitable for the visualization of the microvasculature within bone tissue with or without decalcification (Fig. 2).

The developed decalcifying protocols enable correlative imaging of the same sample with preserved intravascular contrast agent with subsequent classical histological evaluation^[34]. Such a decalcification step enables tomographic imaging of the murine hind limb vasculature with less artifacts around the bone at lower acceleration voltages of the X-ray source due to the reduced radiopacity of the bone. Such lower acceleration voltages often enable shortened scanning times, leading to a higher sample throughput. Furthermore, decalcifying the sample enables a threshold-based segmentation of the vasculature and facilitates histological evaluation of the sample, as both described previously^[34].

Due to the distinct differences in the X-ray attenuation of μ Angiofil and the bone tissue we can also forgo the step of bone decalcification. We thus avoid the need for repeated tomographic scans (before and after decalcification) and subsequent registration of the two scans and are still able to assess vascularization and bone growth directly in one scan. This saves machine and labor time and does not damage the sample composition. The microangioCT approach we present here can thus be used for simultaneous visualization of hard and soft tissues and their vascularization in small and large animal models.

One of the noteworthy possible applications of this approach is simultaneous visualization of the bone microarchitecture and microvasculature of bone metastases in a murine xenograft tumor model (Fig. 3). Especially for studying bone metastatic models it is crucial to find a method that allows for the correct assessment of the microvasculature without decalcifying the sample. Such a decalcification would hinder the thorough assessment of pathological processes in bone tissue. These pathological processes can lead to so-called skeletal-related-events, which are associated with shortened survival and deterioration of quality of life^[41], and should therefore be avoided. Our method allows to study the response to specific treatments, including bone-targeted and antiangiogenic therapies. These can be assessed within the same sample and in 3D, and be followed up with a histological examination if desired^[42]. The presented method could offer additional insights into the interplay between angiogenesis and bone growth, bone lysis, and bone turnover, which have not been fully elucidated yet. The results will be crucial for selecting potential drug candidates and proper treatment decision and efficacy prediction.

In dental research, preclinical models can be divided into small and large animals. Small animal models, particularly mice and rats, are highly popular, due to their practical size and cost-effectiveness. The microCT scan of correspondingly small samples perfused with μ Angiofil can be performed with a voxel size around 1 μ m, providing excellent detail resolution (Fig. 4). Murine mandibles and teeth are challenging for assessing the vasculature. This is due to the location of most

of the vessels within the bone canals or in the proximity of the hard tissue. This consequently leads to the lack of larger bone-free volumes in which the vasculature is easily distinguishable. Gray value based segmentation of bone and contrast-agent-instilled vasculature is compounded by the fact that murine bone has a higher mineral bone density of both cortical and trabecular bone when compared to humans and minipigs^[43]. Nonetheless, with the improved perfusion protocol mentioned above we achieved appropriate imaging of such samples and were able to visualize differences between the X-ray absorption levels of μAngiofil and mineralized bone tissue well.

Nonetheless, the small size of hemimandible samples and availability of the transgenic lines would allow for a recently published imaging approach^[23] in the murine models. This tissue-clearing-based approach could be a viable option for the visualization of the peri-implant tissues and vasculature in small animal models. There are limitations of such a tissue-clearing-based imaging approach, though. Namely i) differential shrinkage among soft and hard tissues, leading to anisotropic distortion in samples where both tissue types (plus eventual metal implant) are present; ii) limited depth (around 800 μm in a mouse model^[23]) due to the challenges of achieving complete transparency of bone tissue. Large anisotropic distortion of the sample may lead to the alteration of the common site of interest, namely the implant-tissue interface. The limitation of the maximal achievable visible depth makes such an approach impractical for usage in large animal models.

Our presented microangioCT approach does not have such limitations and can be easily applied for visualization of hemimandible and its vascularization in a large animal model like Göttingen minipig (Fig. 5). μAngiofil has noticeably different attenuation than mineralized bone and allows for distinct distinction, segmentation and visualization of soft tissue, bone tissue, vessels filled with the contrast agent as well as metal implants according to their gray values in the histogram (Fig. 6).

To the best of our knowledge, ours is the first study demonstrating non-destructive 3D imaging of the microvasculature of bone in the proximity of metal objects/implants in a large animal model.

Limitations of our approach

To achieve the excellent results shown in this study it is paramount that the contrast agent instillation is performed in a reproducible and controlled way. It is thus important that the instillation is performed by skilled personnel, with the help of a syringe pump. Other contrast agents might be slightly easier to use for instillation, but fail to give equally high-quality results, as mentioned above.

Our presented method for the investigation of the microvasculature within the bone tissue is thus mainly limited by the imaging method. Namely, this is the correlation between achievable resolution and the physical size of the imaged sample. If the sample is only a few millimeters in diameter, the voxel sizes in the range of 1 μm enable visualization of the microvasculature down to the capillary bed^[31–34]. In case of large samples, like minipig hemimandible, the achievable voxel size is approximately 10 times larger ($\geq 8 \mu\text{m}$). In such samples the finest microvessels with diameter under 40 μm thus cannot be accurately visualized (see Fig. 5 & 6).

Apart from this general limitation of the tomographic imaging, the hereby presented approach of instilling the vasculature in the bone tissue with a polymerizing contrast agent is a big step forward for qualitative and quantitative imaging. The presented method is suitable to answer important questions regarding the microvasculature in tissue engineering and implantology research as well as many other related research fields.

Author Contributions

[Contributor Roles Taxonomy](#), as defined by the [National Information Standards Organization](#).

Author	Contributions
David Haberthür	Data curation; Formal analysis; Investigation; Project administration; Software; Validation; Visualization; Writing – original draft; Writing – review & editing
Oleksiy-Zakhar Khoma	Data curation; Formal analysis; Investigation; Project administration; Software; Validation; Visualization; Writing – original draft; Writing – review & editing
Tim Hoessly	Data curation; Writing – review & editing
Eugenio Zoni	Investigation; Methodology; Resources; Writing – review & editing
Marianna Kruithof-de Julio	Methodology; Resources; Writing – review & editing
Stewart D. Ryan	Resources; Writing – review & editing
Myriam Grunewald	Investigation; Methodology; Resources; Writing – review & editing
Benjamin Bellón	Investigation; Methodology; Writing – review & editing
Rebecca Sandgren	Investigation; Writing – review & editing
Benjamin E. Pippenger	Funding acquisition; Investigation; Methodology; Resources; Writing – review & editing
Dieter Bosshardt	Methodology; Writing – review & editing
Valentin Djonov	Conceptualization; Funding acquisition; Resources; Writing – review & editing
Ruslan Hlushchuk	Conceptualization; Funding acquisition; Investigation; Methodology; Project administration; Resources; Supervision; Validation; Visualization; Writing – original draft; Writing – review & editing

Conflicts of interest

Author	Conflict
Benjamin Bellón	Employed by a company producing dental implants
Benjamin E. Pippenger	Employed by a company producing dental implants

Acknowledgments

We are grateful to the [Microscopy Imaging Center](#) of the University of Bern for infrastructural support. We thank the `manubot` project^[44] for helping us write this manuscript collaboratively.

Supplementary Materials

Log files of all the tomographic scans performed for this study

The CSV file [ScanningDetails.csv](#) gives a tabular overview of all the (relevant) parameters of all the scans we performed. This file was generated with a [data processing notebook](#) and contains information read from *all* the log files of *all* the scans we performed. A copy of each log file is available [online](#).

References

- [1] [E. Wernike, W. Hofstetter, Y. Liu, G. Wu, H.-J. Sebald, D. Wismeijer, E. B. Hunziker, K.-A. Siebenrock, F. M. Klenke, *J. Biomed. Mater. Res.* **2009**, *9999A*, NA.](#)
- [2] [B. Roche, V. David, A. Vanden-Bossche, F. Peyrin, L. Malaval, L. Vico, M.-H. Lafage-Proust, *Bone* **2012**, *50*, 390.](#)
- [3] C. Carulli, M. Innocenti, M. L. Brandi, *Front. Endocrinol.* **2013**, *4*, DOI [10.3389/fendo.2013.00106](https://doi.org/10.3389/fendo.2013.00106).
- [4] [Y. Ren, J. Senarathna, W. L. Grayson, A. P. Pathak, *American Journal of Physiology-Cell Physiology* **2022**, *323*, C1524.](#)
- [5] [J. Filipowska, K. A. Tomaszewski, Ł. Niedźwiedzki, J. A. Walocha, T. Niedźwiedzki, *Angiogenesis* **2017**, *20*, 291.](#)
- [6] [S. Kuttappan, D. Mathew, J. Jo, R. Tanaka, D. Menon, T. Ishimoto, T. Nakano, S. V. Nair, M. B. Nair, Y. Tabata, *Acta Biomaterialia* **2018**, *78*, 36.](#)
- [7] [T. Kurobane, Y. Shiwaku, T. Anada, R. Hamai, K. Tsuchiya, K. Baba, M. Iikubo, T. Takahashi, O. Suzuki, *Acta Biomaterialia* **2019**, *88*, 514.](#)
- [8] A. Grosso, M. G. Burger, A. Lunger, D. J. Schaefer, A. Banfi, N. Di Maggio, *Front. Bioeng. Biotechnol.* **2017**, *5*, DOI [10.3389/fbioe.2017.00068](https://doi.org/10.3389/fbioe.2017.00068).
- [9] [M. Lovett, K. Lee, A. Edwards, D. L. Kaplan, *Tissue Engineering Part B: Reviews* **2009**, *15*, 353.](#)
- [10] J. A. Núñez, A. Goring, E. Hesse, P. J. Thurner, P. Schneider, C. E. Clarkin, *Sci Rep* **2017**, *7*, DOI [10.1038/s41598-017-13632-5](https://doi.org/10.1038/s41598-017-13632-5).
- [11] A. N. Rindone, X. Liu, S. Farhat, A. Perdomo-Pantoja, T. F. Witham, D. L. Coutu, M. Wan, W. L. Grayson, *Nat Commun* **2021**, *12*, DOI [10.1038/s41467-021-26455-w](https://doi.org/10.1038/s41467-021-26455-w).
- [12] [W. Luo, Y. Yi, D. Jing, S. Zhang, Y. Men, W.-P. Ge, H. Zhao, *Stem Cells and Development* **2019**, *28*, 1310.](#)
- [13] [Á. E. Mercado-Pagán, A. M. Stahl, Y. Shanjani, Y. Yang, *Ann Biomed Eng* **2015**, *43*, 718.](#)
- [14] K. D. Harrison, D. M. L. Cooper, *Front. Endocrinol.* **2015**, *6*, DOI [10.3389/fendo.2015.00122](https://doi.org/10.3389/fendo.2015.00122).
- [15] [P. Schneider, T. Krucker, E. Meyer, A. Ullmann-Schuler, B. Weber, M. Stampanoni, R. Müller, *Microsc. Res. Tech.* **2009**, *72*, 690.](#)
- [16] [S. Young, J. D. Kretlow, C. Nguyen, A. G. Bashoura, L. S. Baggett, J. A. Jansen, M. Wong, A. G. Mikos, *Tissue Engineering Part B: Reviews* **2008**, *14*, 295.](#)
- [17] [T. Krucker, A. Lang, E. P. Meyer, *Microsc. Res. Tech.* **2006**, *69*, 138.](#)
- [18] D. S. Perrien, M. A. Saleh, K. Takahashi, M. S. Madhur, D. G. Harrison, R. C. Harris, T. Takahashi, *BMC Nephrol* **2016**, *17*, DOI [10.1186/s12882-016-0235-5](https://doi.org/10.1186/s12882-016-0235-5).
- [19] [L. Leyssens, C. Pestiaux, G. Kerckhofs, *IJMS* **2021**, *22*, 3263.](#)
- [20] [S. Hong, A. M. Herman, J. M. Stephenson, T. Wu, A. N. Bahadur, A. R. Burns, S. P. Marrelli, J. D. Wythe, *J. Neurosci Res* **2019**, *98*, 312.](#)

- [21] [R. Hlushchuk, S. Barré, V. Djonov, in *Methods in Molecular Biology*, Springer New York, **2016**, pp. 13–24.](#)
- [22] [X. L. Jing, A. S. Farberg, L. A. Monson, A. Donneys, C. N. Tchanque-Fossuo, S. R. Buchman, *Craniomaxillofacial Trauma & Reconstruction* **2012**, *5*, 223.](#)
- [23] [Y. Yi, Y. Men, D. Jing, W. Luo, S. Zhang, J. Q. Feng, J. Liu, W. Ge, J. Wang, H. Zhao, *Cell Prolif* **2019**, *52*, e12578.](#)
- [24] [J. Raphael, M. Holodniy, S. B. Goodman, S. C. Heilshorn, *Biomaterials* **2016**, *84*, 301.](#)
- [25] J. Hsieh, *Computed Tomography: Principles, Design, Artifacts, and Recent Advances*, SPIE Optical Engineering Press, Bellingham, WA, **2003**.
- [26] [L. Bai, Y. Liu, Z. Du, Z. Weng, W. Yao, X. Zhang, X. Huang, X. Yao, R. Crawford, R. Hang, D. Huang, B. Tang, Y. Xiao, *Acta Biomaterialia* **2018**, *76*, 344.](#)
- [27] [S. Wang, Y. Liu, D. Fang, S. Shi, *Oral Diseases* **2007**, *13*, 530.](#)
- [28] [A. Pearce, R. Richards, S. Milz, E. Schneider, S. Pearce, *eCM* **2007**, *13*, 1.](#)
- [29] [D. Bellinger, E. Merricks, T. Nichols, in *The Minipig in Biomedical Research*, CRC Press, **2011**, pp. 445–468.](#)
- [30] M. Grunewald, S. Kumar, H. Sharife, E. Volinsky, A. Gileles-Hillel, T. Licht, A. Permyakova, L. Hinden, S. Azar, Y. Friedmann, P. Kupetz, R. Tzuberi, A. Anisimov, K. Alitalo, M. Horwitz, S. Leebhoff, O. Z. Khoma, R. Hlushchuk, V. Djonov, R. Abramovitch, J. Tam, E. Keshet, *Science* **2021**, *373*, DOI [10.1126/science.abc8479](https://doi.org/10.1126/science.abc8479).
- [31] [R. Hlushchuk, D. Haberthür, P. Soukup, S. F. Barré, O.-Z. Khoma, J. Schitny, N. Haghayegh Jahromi, A. Bouchet, B. Engelhardt, V. Djonov, *Brain Struct Funct* **2020**, *225*, 2885.](#)
- [32] [R. Hlushchuk, C. Zubler, S. Barré, C. Correa Shokiche, L. Schaad, R. Röthlisberger, M. Wnuk, C. Daniel, O. Khoma, S. A. Tschanz, M. Reyes, V. Djonov, *American Journal of Physiology-Renal Physiology* **2018**, *314*, F493.](#)
- [33] [R. Hlushchuk, D. Haberthür, V. Djonov, *Vascular Pharmacology* **2019**, *112*, 2.](#)
- [34] L. Schaad, R. Hlushchuk, S. Barré, R. Gianni-Barrera, D. Haberthür, A. Banfi, V. Djonov, *Sci Rep* **2017**, *7*, DOI [10.1038/srep41842](https://doi.org/10.1038/srep41842).
- [35] [E. Zoni, L. Astrologo, C. K. Y. Ng, S. Piscuoglio, J. Melsen, J. Grosjean, I. Klima, L. Chen, E. B. Snaar-Jagalska, K. Flanagan, G. van der Pluijm, P. Kloen, M. G. Cecchini, M. Kruithof-de Julio, G. N. Thalmann, *Molecular Cancer Research* **2019**, *17*, 1049.](#)
- [36] J. Dai, J. Hensel, N. Wang, M. Kruithof-de Julio, Y. Shiozawa, *BoneKEy Reports* **2016**, *5*, DOI [10.1038/bonekey.2016.4](https://doi.org/10.1038/bonekey.2016.4).
- [37] [Y. Li, D. Fraser, J. Mereness, A. Van Hove, S. Basu, M. Newman, D. S. W. Benoit, *ACS Appl. Bio Mater.* **2021**, *5*, 20.](#)
- [38] [N. G. Schott, N. E. Friend, J. P. Stegemann, *Tissue Engineering Part B: Reviews* **2021**, *27*, 199.](#)
- [39] [K. K. Sivaraj, R. H. Adams, *Development* **2016**, *143*, 2706.](#)
- [40] [P. Chandra, A. Atala, *Clinical Science* **2019**, *133*, 1115.](#)
- [41] [S. D'Oronzo, R. Coleman, J. Brown, F. Silvestris, *Journal of Bone Oncology* **2019**, *15*, 100205.](#)

- [42] [H. Xu, M.-H. Lafage-Proust, L. Bouazza, S. Geraci, P. Clezardin, B. Roche, F. Peyrin, M. Langer, *Cancers* **2022**, *14*, 3443.](#)
- [43] [V. Entezari, V. Vartanians, D. Zurakowski, N. Patel, R. J. Fajardo, R. Müller, B. D. Snyder, A. Nazarian, *Bone* **2012**, *50*, 611.](#)
- [44] [D. S. Himmelstein, V. Rubinetti, D. R. Slochower, D. Hu, V. S. Malladi, C. S. Greene, A. Gitter, *PLoS Comput Biol* **2019**, *15*, e1007128.](#)